

## Stability and scalability of piezoelectric flags

Xiaolin Wang, Silas Alben, Chenyang Li, and Yin Lu Young

Citation: [Physics of Fluids](#) **28**, 023601 (2016); doi: 10.1063/1.4940990

View online: <http://dx.doi.org/10.1063/1.4940990>

View Table of Contents: <http://aip.scitation.org/toc/phf/28/2>

Published by the [American Institute of Physics](#)

---

### Articles you may be interested in

[Hydroelastic response and energy harvesting potential of flexible piezoelectric beams in viscous flow](#)

[Physics of Fluids](#) **24**, 054106 (2012); 10.1063/1.4719704

[Resonance-induced enhancement of the energy harvesting performance of piezoelectric flags](#)

[Applied Physics Letters](#) **107**, 263901 (2015); 10.1063/1.4939117

[Dynamics of an inverted flexible plate in a uniform flow](#)

[Physics of Fluids](#) **27**, 073601 (2015); 10.1063/1.4923281

[Role of mass on the stability of flag/flags in uniform flow](#)

[Applied Physics Letters](#) **103**, 034101 (2013); 10.1063/1.4813006

[Numerical and experimental investigation of natural flow-induced vibrations of flexible hydrofoils](#)

[Physics of Fluids](#) **28**, 075102 (2016); 10.1063/1.4954785

[Piezoelectric energy harvesting in coupling-chamber excited by the vortex-induced pressure](#)

[Applied Physics Letters](#) **109**, 073902 (2016); 10.1063/1.4961528

---



**COMPLETELY  
REDESIGNED!**

**PHYSICS  
TODAY**

*Physics Today Buyer's Guide*  
Search with a purpose.

## Stability and scalability of piezoelectric flags

Xiaolin Wang,<sup>1,a)</sup> Silas Alben,<sup>1,a)</sup> Chenyang Li,<sup>2,a)</sup> and Yin Lu Young<sup>2,a)</sup>

<sup>1</sup>*Department of Mathematics, University of Michigan, Ann Arbor, Michigan 48109, USA*

<sup>2</sup>*Department of Naval Architecture and Marine Engineering, University of Michigan, Ann Arbor, Michigan 48109, USA*

(Received 18 September 2015; accepted 18 January 2016; published online 9 February 2016)

We investigate the effect of piezoelectric material on the flutter speed, vibration mode and frequency, and energy harvesting power and efficiency of a flexible flag in various fluids. We develop a fully coupled fluid-solid-electric model by combining the inviscid vortex sheet model with a linear electro-mechanical coupling model. A resistance only circuit and a resonant resistance-inductance (RL) circuit are considered. For a purely resistive circuit, an increased electro-mechanical coupling factor results in an increased flutter speed, vibration frequency, averaged electric power, and efficiency. A consistent optimal resistance is found that maximizes the flutter speed and the energy harvesting power. For a resonant RL circuit, by tuning the inductance to match the circuit frequency to the flag's vibration frequency, the flutter speed can be greatly decreased, and a larger averaged power and efficiency are obtained. We also consider a model scale setup with several commonly used commercial materials for operating in air and water. Typical ranges of dimensionless parameters are obtained for four types of material that span a wide range of solid density and rigidity values. We find that the resistance only circuit is more effective when the flag is placed in a lighter fluid (e.g., air), while the RL circuit is able to reduce the flutter speed when the flag is placed in a heavier fluid (e.g., water). © 2016 AIP Publishing LLC. [<http://dx.doi.org/10.1063/1.4940990>]

### I. INTRODUCTION

Piezoelectric material (for example, PZT) has drawn enormous attention in recent decades due to its ability to convert mechanical kinetic energy into electrical potential energy, and vice versa. It has been applied to energy harvesting devices to power micro sensors/actuators,<sup>1,2</sup> and to passively control structural vibrations.<sup>3-5</sup> The fundamental mechanism in the electro-mechanical process requires vibrations of the solid, which can be realized through natural flow-induced vibrations.

A flexible elastic flag undergoes flow-induced vibration through the competition between the destabilizing effect of the fluid pressure and the stabilizing effect of the flag's internal bending rigidity. In particular, the flag will develop large-amplitude deformations if the flow speed is above a certain critical value, which we define as flutter. Much previous work has been conducted on this phenomenon through experiments,<sup>6-11</sup> inviscid and viscous numerical simulations,<sup>12-19</sup> and linear stability analysis.<sup>11,20,21</sup> The critical flutter speed was found over a large range of mass ratio (ratio of solid to fluid inertial force), and increases as the mass ratio decreases. The effect of mass ratio on the flutter mode was observed in experiments and numerical simulations, and both found that the flag flutters in higher modes when the mass ratio decreases and the first mode shape is never unstable for a cantilever plate.<sup>12,21</sup> Post-flutter behavior was also discussed in previous work, and flags were found to transition from limit-cycle oscillations to more chaotic states as the fluid velocity increases beyond flutter.<sup>16,22,23</sup>

The objective of this work is to consider the effect of the piezoelectric material on the flutter speed, vibration mode and frequency, and energy harvesting power and efficiency of a flexible

---

<sup>a)</sup>Electronic addresses: [wxiaolin@umich.edu](mailto:wxiaolin@umich.edu); [alben@umich.edu](mailto:alben@umich.edu); [licheny@umich.edu](mailto:licheny@umich.edu); and [ylyoung@umich.edu](mailto:ylyoung@umich.edu).

flag. Previous studies found that the electro-mechanical coupling effect of the piezoelectric material acts to increase the bending stiffness of the system, and therefore will tend to stabilize the flag by increasing the critical flutter speed.<sup>19,24</sup> The output circuit also has an important impact on the flutter boundary. It is often described as a shunting circuit as the piezoelectric material is modeled as a current source in parallel with its internal capacitance,<sup>25,26</sup> and the output circuit provides extra paths for the current. A resistive shunting circuit with a single resistor and a resonance shunting circuit with resistor-inductor (RL) are two commonly used output circuits for energy harvesting and vibration control.<sup>3</sup> With the resistive shunting, Akcabay and Young<sup>19</sup> studied the fluid-solid interaction of a bimorph piezoelectric cantilevered beam in a viscous flow using the immersed boundary method, and they found an optimal resistance value for energy harvesting efficiency. Michelin and Doaré<sup>24</sup> studied the piezoelectric coupling effect on the local and global instabilities, as well as on energy conversion efficiency for a flexible plate using the double wake inviscid model. They found that the critical flutter speed increases as the piezoelectric coupling increases, and the energy conversion efficiency depends on piezoelectric coupling, loaded resistance, and the thickness ratio of the PZT patch to the substrate material. In another work, they studied bodies of small span using slender body theory.<sup>27</sup> The increase of the flutter speed by the PZT material has an important impact on vibration control. On the other hand, higher effective system stiffness also indicates the flutter initiates at a larger flow speed, which will impact the energy harvesting potential and efficiency. In one aspect, this limits the effectiveness of the piezoelectric material in energy harvesting, especially in water and other heavier fluids because the required flutter speed is higher when the solid-to-fluid mass ratio is smaller. Some recent work suggests that this difficulty may be overcome by connecting the PZT flag to a well-tuned resonant shunting circuit. Xia *et al.*<sup>28</sup> found that the flag's vibrating frequency can lock-in to the circuit resonant frequency for a parallel connected RL circuit using the slender body theory. They showed a significantly enhanced energy efficiency and a large decrease of the flutter speed in the lock-in regime. Similar results were obtained for the passive control of vibrating plates. Li *et al.*<sup>29</sup> investigated the effect of the RL circuit on the passive control of a hydrofoil. They also observed a maximum damping enhancement for an open-loop vibration control application via PZT with a RL circuit when the inductor is tuned to match the circuit resonant frequency with the foil resonant frequency.

In this work, we extend the vortex-sheet model by Alben<sup>30</sup> and include the piezoelectric effect by addition of a linear electro-mechanical coupling model for a fully coupled model. We use the model to predict the electro-fluid-solid response of a piezoelectric flag connected with an output electric circuit in incompressible and inviscid flow. In this model, the vortex layers induced by the body tend to sheets of infinitesimal thickness. A vortex-sheet model is efficient for slightly viscous flow because it can present the flow using vortex sheet, which is only one-dimensional in a 2D flow. It allows flow separations at prescribed locations only (usually sharp edges), but it agrees quantitatively with Navier-Stokes models in predicting the strength of shed circulation, and the location of the primary vortices in the wake of an oscillated plate.<sup>31</sup> Previous work also shows a good agreement of the vortex-sheet model in predicting the stability boundary of a flapping flag.<sup>16</sup> In this work, we assume the ambient fluid dynamics are 2D, as in some of the previous studies<sup>12,15,17,19,24</sup> which apply to flags of large aspect ratios. Slender body theory<sup>27,32</sup> as well as other 3D models<sup>21,33,34</sup> have been used in the limit of small aspect ratios. In general, the flutter velocity increases as the aspect ratio decreases.<sup>21,34</sup> Asymmetric flapping motion is also observed when the Reynolds number is large due to 3D effects.<sup>33</sup> In spite of the differences between the 2D and 3D models, the behavior of the flutter velocity with respect to the mass ratio and other parameters is qualitatively similar for different aspect ratios.<sup>32</sup> Linear electro-mechanical coupling models were applied to cantilever flags for a single-patch PZT layer model<sup>35,36</sup> and a multiple-patch layer<sup>24,37</sup> model, and were found to compare well with experimental results at low to moderate strains. We then derive the important dimensionless parameters that govern the model, and investigate their effects on the critical flutter speed, vibration frequency, mode shapes, and energy harvesting power and efficiency with the numerical simulation results. Next, we discuss the effectiveness and scalability of bimorph PZT flags for energy harvesting and vibration control applications in air versus in water and for different substrate materials.

The paper is organized as follows: Sec. II describes the vortex-sheet-plate model for the piezoelectric flag; Sec. III studies the effects of piezoelectric parameters on the stability boundary; Sec. IV presents the scalability results for actual devices with different materials and fluids. The conclusions are presented in Sec. V.

## II. MODELLING

### A. Plate-vortex-sheet model

We consider here the motion of a cantilevered thin plate or beam in an inviscid flow. The beam is of chord length  $C$ , span length  $S$ , mass per unit chordwise length  $m_s$ , and bending rigidity  $B$ . The flow and the motion of the beam are assumed to be 2D, so all the properties are uniform in the spanwise direction. The thickness of the beam is assumed to be much smaller than its chord and span, so we model it as a 1D inextensible elastic sheet. Piezoelectric layers are combined in parallel on both sides of the beam by poling the layers in the same direction.<sup>35,38</sup> The beam moves under the pressure forces of a surrounding inviscid and incompressible flow of density (mass per unit volume)  $\rho_f$  with a uniform upstream horizontal velocity  $U$ . A schematic figure of the piezoelectric beam is shown in Figure 1(a).

The instantaneous position of the beam is described as  $\zeta(s,t) = x(s,t) + iy(s,t)$ , where  $s$  is the arclength. Assuming an Euler-Bernoulli model for the plate, the bending moment at a given position consists of an internal rigidity of the material and the piezoelectric coupling,

$$M(s,t) = B\kappa(s,t) - \beta_M V(s,t), \quad (1)$$

where  $B = EI$  is the bending rigidity with  $E$  the material's Young's modulus and  $I$  its second moment of area,  $\kappa(s,t)$  is the curvature of the beam,  $\beta_M$  is an electro-mechanical coupling factor indicating the bending moment generated per unit voltage, and  $V(s,t)$  is the electric potential difference generated across the piezoelectric layers. Here positive voltage induces a positive curvature of the beam, by the sign in front of  $\beta_M$  in Equation (1). The sign is set by the initial preparation (poling) of the material. Therefore, the governing equation for  $\zeta$  is

$$m_s \partial_{tt} \zeta(s,t) = \partial_s (T(s,t) \hat{s}) - B \partial_s (\partial_s \kappa(s,t) \hat{n}) + \beta_M \partial_s (\partial_s V(s,t) \hat{n}) - S[p](s,t) \hat{n}. \quad (2)$$

Here,  $T(s,t)$  is the beam's tension force accounting for its inextensibility, and  $[p](s,t)$  is the pressure jump across the beam.  $\hat{s} = \partial_s \zeta$  and  $\hat{n} = i\hat{s}$  represent the unit tangent and normal vectors to the beam, respectively.

The piezoelectric material can be represented as a current source in parallel with its internal capacitance,<sup>25,26</sup> and the surface density of the current is modeled as  $-\beta_M \partial_t \kappa$  in the linear electro-mechanical coupling.<sup>35</sup> The piezoelectric composite beam is connected in parallel with a RL output circuit. Therefore, Kirchoff's current law can be applied to the electrical circuit shown in

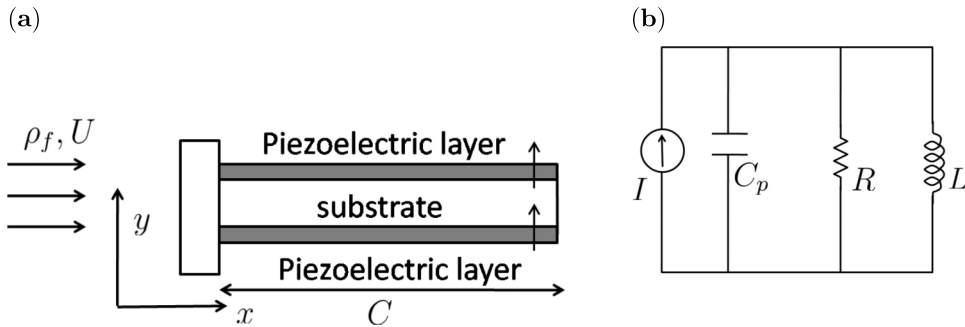


FIG. 1. (a) A cantilever beam of chord length  $C$  subject to a uniform flow of speed  $U$  and density  $\rho_f$ . The arrows on the piezoelectric layer indicate the two layers are poled in the same direction. (b) Equivalent circuit parallel connected with a resistor.  $R$  is the resistance,  $L$  is the inductance,  $C_p$  is the equivalent capacitance of the PZT material,  $I$  is the current generated by electro-mechanical conversion effect.

Figure 1(b) to obtain the constitutive equation,

$$c_p \partial_{tt} V + \frac{\partial_t V}{r} + \frac{V}{l} + \beta_M \partial_{tt} \kappa = 0, \quad (3)$$

where  $c_p = \frac{C_p}{C}$ ,  $r = RC$ , and  $l = LC$  are the surface density of the internal capacitance, resistance, and inductance, respectively, with  $C$  as the chord length of the beam. This equation has been used in previous work by Xia *et al.*<sup>28</sup> Since the piezoelectric layer is parallel connected, the value of capacitance is twice that on each layer. The piezoelectric effect also plays a role in the trailing edge condition, where the pressure induced moment and forces are zero,

$$T = \partial_s \kappa = 0, \quad \kappa = \frac{\beta_M}{B} V. \quad (4)$$

In other works, the voltage  $V = V(t)$  is modeled as a constant along the piezoelectric layer,<sup>19,35,39</sup> then the above Equation (3) can be rewritten by integrating along the arclength,

$$C_p \partial_{tt} V + \frac{\partial_t V}{R} + \frac{V}{L} + \beta_M \int_0^C \partial_{tt} \kappa(s', t) ds' = 0. \quad (5)$$

In this formulation,  $\beta_M \partial_s (\partial_s V(s, t) \hat{n}) = 0$ , Equation (2) then reduces to the Bernoulli beam equation,<sup>30</sup> i.e., without piezoelectric effect. In this case, the piezoelectric material affects the flag only through the boundary condition, and we can view the piezoelectric material as adding an extra concentrated moment at the free tip of the beam.

The pressure forces are computed by the inviscid vortex-sheet model described by Alben.<sup>30</sup> In the vortex-sheet model, the flow is computed in terms of the position and strength of a single vortex sheet. The vortex sheet consists of a “bound” part ( $C_b$ ) on the beam, and it separates from the beam’s trailing edge into a “free” part ( $C_f$ ). The position of the vortex sheet is denoted  $\zeta(s, t)$ , which is the same as the beam’s position when  $0 \leq s \leq C$ . The strength of the vortex sheet is denoted  $\gamma(s, t)$ , which is also the jump in tangential velocity of the beam. On the bound vortex sheet, the flow satisfies the no-penetration condition, which requires the body’s normal velocity to equal the flow’s normal velocity,

$$Re(\hat{n} \partial_t \zeta^*) = Re \left( \hat{n} \left( U + \frac{1}{2\pi i} \int_{C_b} \frac{\gamma(s', t)}{\zeta(s, t) - \zeta(s', t)} ds' + b_\delta(s, t) \right) \right), \quad \zeta(s, t) \in C_b. \quad (6)$$

Here, the symbol “\*” denotes complex conjugate and  $U$  is the speed of the incoming flow. The special integral symbol in the equation denotes a principal-value integral, and the general solution  $\gamma(s, t)$  has inverse-square-root singularities at the beam’s leading and trailing edge.<sup>40</sup> The last term is a regularized Biot-Savart integral using the smoothing parameter  $\delta$  of Krasny’s method.<sup>41</sup>

$$b_\delta(s, t) = \frac{1}{2\pi i} \int_{C_f} \frac{\zeta^*(s, t) - \zeta^*(s', t)}{|\zeta(s, t) - \zeta(s', t)|^2 + \delta(s', t)^2} ds', \quad \zeta(s, t) \in C_f, \quad (7)$$

where

$$\delta(s, t) = \delta_0 (1 - \exp(-|\zeta(L, t) - \zeta(s, t)|^2 / 4\delta_0^2)) \quad (8)$$

with  $\delta_0 = 0.2$ . This tapered regularization decreases the effect of the regularization term at the trailing edge as  $\delta(s, t) \rightarrow 0$  with  $s \rightarrow C$ , and it allows smooth vorticity and velocity dynamics for the free vortex sheet.<sup>42</sup>

On the free sheet  $C_f$  in the wake, the vortex sheet evolves according to the Birkhoff-Rott equation:<sup>43,44</sup>

$$\frac{\partial \zeta^*}{\partial t}(s, t) = U + \frac{1}{2\pi i} \int_{C_b} \frac{\gamma(s', t)}{\zeta(s, t) - \zeta(s', t)} ds' + b_\delta(s, t), \quad \zeta(s, t) \in C_f. \quad (9)$$

The pressure jump  $[p](s, t)$  across the beam is related to the vortex sheet strength  $\gamma(s, t)$  using a version of the unsteady Bernoulli equation:<sup>45-47</sup>

$$\gamma_t(s, t) + \partial_s((\tau_f(s, t) - \tau_s(s, t))\gamma(s, t)) = \frac{1}{\rho_f} \partial_s [p](s, t). \quad (10)$$

TABLE I. Dimensionless parameters governing the piezoelectric flexible beam.

Dimensionless group			Physical meaning
Mass ratio	$\bar{M}$	$\frac{m_s}{\rho_f b S}$	Ratio of the solid inertia to fluid inertia
Reduced velocity	$\bar{U}$	$U \sqrt{\frac{\rho_f b^3 S}{B}}$	Ratio of the fluid kinetic energy to the solid elastic energy
Piezoelectric/mechanical coupling factor	$\bar{\beta}_M$	$\beta_M \sqrt{\frac{1}{B c_p}}$	Ratio of the stored electrical energy in PZT to the solid elastic energy
Reduced resistance density	$\bar{r}$	$r c_p \sqrt{\frac{B}{\rho_f b^3 S}}$	Ratio of the produced energy dissipated in resistance and stored as elastic energy to fluid kinetic energy
Reduced circuit frequency	$f_e$	$\frac{1}{2\pi} \sqrt{\frac{\rho_f b^5 S}{l c_p B}}$	Ratio of the produced energy stored in inductance and stored as elastic energy to fluid kinetic energy

Here,  $\tau_f(s, t)$  and  $\tau_s(s, t)$  are the tangential velocities of the fluid and the solid, respectively. We couple equations (2), (3), (6), (9), and (10) together and solve the nonlinear system with a numerical method similar to Alben's work.<sup>30</sup> We compute the free vortex sheet with an explicit method and solve for the unknown variables including beam position, vortex sheet strength, pressure, and voltage using Broyden's method.<sup>48</sup> More detailed discussion can be found in previous work,<sup>30</sup> including how the vorticity in the free vortex sheet is generated at the trailing edge using the Kutta condition, and how the Chebyshev-Lobatto nodes are implemented to improve the convergence of integral-type equation.

## B. Nondimensionalization

We nondimensionalize the governing equations by the semi-chord  $b = \frac{1}{2}C$ , the fluid density  $\rho_f$ , and the internal capacitance density  $c_p$ . We choose the velocity scale as  $u = \sqrt{\frac{B}{\rho_f b^3 S}}$  so that the dimensionless inflow velocity is  $\bar{U} = U \sqrt{\frac{\rho_f b^3 S}{B}}$  and  $\bar{U}^2$  represents the ratio of the fluid kinetic energy to the solid elastic energy. Therefore, we have the characteristic time as  $\tau = \frac{b}{u} = \sqrt{\frac{\rho_f b^5 S}{B}}$ , and the following dimensionless variables:

$$\bar{\zeta} = \frac{\zeta}{b}, \quad \bar{t} = \frac{t}{\tau}, \quad \bar{\kappa} = \kappa b, \quad \bar{T} = T \frac{b^2}{B}, \quad \bar{p} = p \frac{b^3 S}{B}, \quad \bar{V} = V \sqrt{\frac{c_p b^2}{B}}, \quad \bar{f} = f \sqrt{\frac{\rho_f b^5 S}{B}}.$$

Here,  $f$  is the beam vibration frequency. We list the dimensionless parameters and the corresponding physical meanings in Table I.

Instead of the reduced inductance  $\bar{l}$ , we use the resonant frequency of the RL circuit  $f_e = 1/2\pi\sqrt{\bar{l}}$  to characterize the inductive property of the circuit. We then obtain the following dimensionless equations:

$$\bar{M} \partial_{\bar{t}\bar{t}} \bar{\zeta}(\bar{s}, \bar{t}) = \partial_{\bar{s}}(\bar{T} \hat{s}) - \partial_{\bar{s}}(\partial_{\bar{s}} \bar{\kappa} \hat{n}) + \bar{\beta}_M \partial_{\bar{s}}(\partial_{\bar{s}} \bar{V} \hat{n}) - [\bar{p}] \hat{n}, \quad (11)$$

$$\partial_{\bar{t}\bar{t}} \bar{V} + \frac{\partial_{\bar{t}} \bar{V}}{\bar{f}} + 4\pi^2 \bar{f}_e^2 \bar{V} + \bar{\beta}_M \partial_{\bar{t}\bar{t}} \bar{\kappa} = 0. \quad (12)$$

## III. RESULTS

### A. Validation of flutter velocity and frequency without piezoelectric effect

We first briefly review the flutter boundary for flags in an unbounded flow without the piezoelectric effect. The flag deformation grows exponentially when the speed of the background flow exceeds the flutter speed.<sup>11</sup> The flutter boundary curve gives the parameter values at which the

net damping of the beam becomes zero. In the simulation, it is obtained by imposing small initial deflection and tracking the deflection's growth or decay in time. Below the curve that represents the flutter boundary (in  $\bar{U}$ ), the initial perturbation on the beam will decay in time to zero due to the net positive damping; above the curve, small perturbations will grow exponentially due to net negative damping.

In Figure 2(a), we show the reduced flutter speed  $\bar{U}$  for beams for a large range of mass ratios  $\bar{M}$  together with the previous experimental, numerical, and analytical results, where all are obtained without the piezoelectric effect.

In general, our inviscid vortex sheet model consistently underestimates the critical flutter speed compared to the viscous and the experimental results. Viscous effect increases the axial tension on the flag.<sup>19</sup> By considering the boundary layer drag on a flat plate,<sup>49</sup> the tension can be approximated,<sup>11</sup> in terms of Reynolds number ( $Re$ ), to scale as  $Re^{-1/2}$ . The beam tension will stabilize the system and therefore increase the flutter velocity slightly at large  $Re$ . Another factor that leads to the discrepancy between our work and the experimental results is that we neglect material damping in our model. Typical beams have a material damping coefficient of 1%–5%,<sup>50</sup> and previous work shows that increases in material damping will lead to a delay in flutter, particularly for large  $\bar{M}$ .<sup>19</sup> The vortex sheet model agrees well with other inviscid model results, especially in the low mass ratio regime ( $\bar{M} < 1$ ). When  $\bar{M}$  is large, the beam flutters at lower mode in the flapping state, and the assumption that its shape is close to a travelling wave in Shelley's infinite flag model<sup>11</sup> is violated. Therefore, we observe a large discrepancy between the solid line (current model) and the dashed line (Shelley's model) for  $\bar{M} > 1$  in panel (a) of Figure 2. We also notice differences in the flutter boundary between our model and the inviscid results from Eloy *et al.*<sup>21</sup> and Tang and Poidoussis.<sup>17</sup> Eloy *et al.* used a “double wake” model, which has an artificial upstream wake, while our model only includes the wake shed from the trailing edge. This leads to different flow descriptions, especially for heavier beam  $\bar{M} > 1$ . Tang and Poidoussis used a vortex panel method and modeled the vortex wake as a series of vortices whose strength depends on the Kutta-condition. They also included 0.4% material damping in the model, which could be the reason that their flutter boundary curve is closer to the experimental results by Huang.<sup>7</sup>

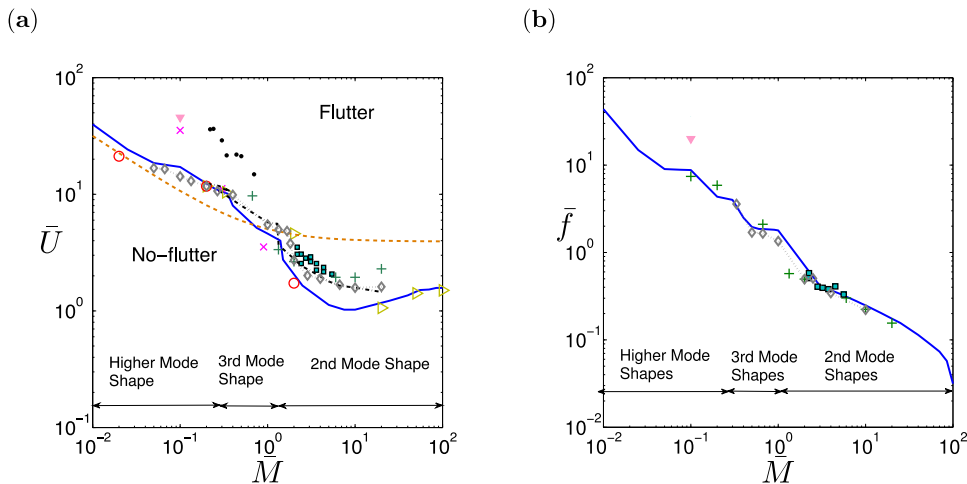


FIG. 2. (a) Flutter velocity  $\bar{U}$  at different mass ratio  $\bar{M}$ . (b) Response frequency  $\bar{f}$  at the flutter boundary with different mass ratio  $\bar{M}$ . Current inviscid plate-vortex sheet method (solid line). Experimental results by Watanabe *et al.*<sup>9</sup> conducted in air at  $Re \approx 100\,000$  ( $\bullet$ ), Huang<sup>7</sup> conducted in air at  $Re \approx 40\,000$  ( $\blacksquare$ ), Shelley *et al.*<sup>11</sup> conducted in water at  $Re \approx 60\,000$  ( $\blacktriangledown$ ). Numerical simulation results of viscous flow model by Akcabay and Young<sup>19</sup> at  $Re = 840$  ( $+$ ), Connell and Yue<sup>15</sup> at  $Re = 1000$  ( $\times$ ). Numerical simulation results of inviscid flow model by Tang and Poidoussis<sup>17</sup> with potential flow theory (dotted-diamond line), Michelin *et al.*<sup>18</sup> with point vortex model ( $\triangleright$ ), Do re and Michelin<sup>24</sup> with double wake model ( $\circ$ ). Inviscid analytical results by Shelley *et al.*<sup>11</sup> with infinite flag model (dashed line), Eloy *et al.*<sup>21</sup> with double wake model and linear stability analysis (dashed-dotted line).

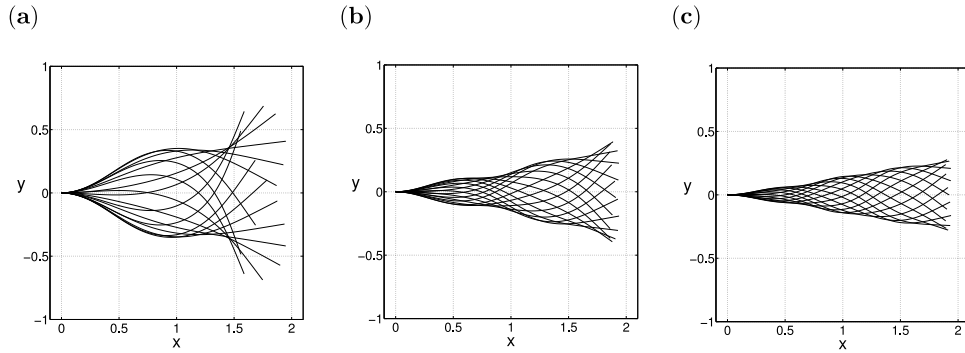


FIG. 3. Flag snapshots corresponding to different modes of beam oscillations just above the flutter boundary. (a) Second mode shape,  $\bar{M} = 4$  and  $\bar{U} = 1.4$ . (b) Third mode shape,  $\bar{M} = 0.6$  and  $\bar{U} = 6$ . (c) Fourth mode shape,  $\bar{M} = 0.2$  and  $\bar{U} = 12$ .

In panel (b) of Figure 2, we show the flapping frequency  $\bar{f}$  of the beam at the flutter boundary. The velocity is chosen to be right above the flutter boundary according to panel (a). Our results agree well with previous numerical and experimental results.

In the flapping state, the flag shows different mode structures which are determined by the most unstable mode. This phenomenon is observed in experiments,<sup>9,21</sup> simulations,<sup>17–19</sup> and linear stability analysis.<sup>20,21</sup> In Figure 3, we show the typical mode shapes of the beam oscillations just above the flutter boundary. If we define the mode shape by the number of necks in the flags' envelopes similarly to the work of Michelin *et al.*,<sup>18</sup> we obtain flapping modes ranging from 2 (one neck) and 3 (two necks) to higher values depending on the mass ratio  $\bar{M}$ . A sharp change of flutter velocity and flapping frequency is observed when the flag changes its mode shape as shown in Figure 2. When  $\bar{M}$  is small, the relative dominance of fluid inertia and high beam flexibility at the flutter boundary allow higher wavenumber bending. This observation is in agreement with previous work.<sup>9,18,19</sup>

## B. Influence of piezoelectric material on flutter

Now we consider the effect of the piezoelectric material on flutter. With the piezoelectric material, the effective system stiffness is increased by decreasing the fluid disturbing moment via the electro-mechanical coupling term with  $\bar{\beta}_M$  in Equation (1). This term dissipates fluid kinetic energy through the output circuit. Overall, the piezoelectric material functions as a stabilizer to the system by increasing the effective stiffness and damping.

### 1. Piezoelectric effects without inductance

We first consider a simpler circuit without the inductor. In this case, the circuit equation becomes

$$\partial_t \bar{V} + \frac{\bar{V}}{\bar{f}} + \bar{\beta}_M \partial_t \bar{k} = 0. \quad (13)$$

In Figure 4, we plot the critical flutter speed and the corresponding response frequency right on the flutter boundary. The dimensionless parameter  $\bar{\beta}_M$  is determined by the properties of the piezoelectric material and the geometry of the beam. For example, the sample result of  $\bar{\beta}_M$  for a PZT-5H beam with a chord-to-span ratio of 1 and thick-to-chord ratio of 0.0002 is around 0.26 (more details are discussed in Section IV). The  $\bar{\beta}_M$  values chosen in this work are all practical values that can be realized by certain commonly used piezoelectric materials. We define the flutter velocity to be  $U_0$  and the flutter frequency to be  $f_0$  when the piezoelectric material is not included, and plot them with solid lines in Figure 4. The flutter velocity increases when  $\bar{\beta}_M$  increases for a given  $\bar{f}$ . The piezoelectric material not only affects the flutter boundary, but also changes the vibration frequency

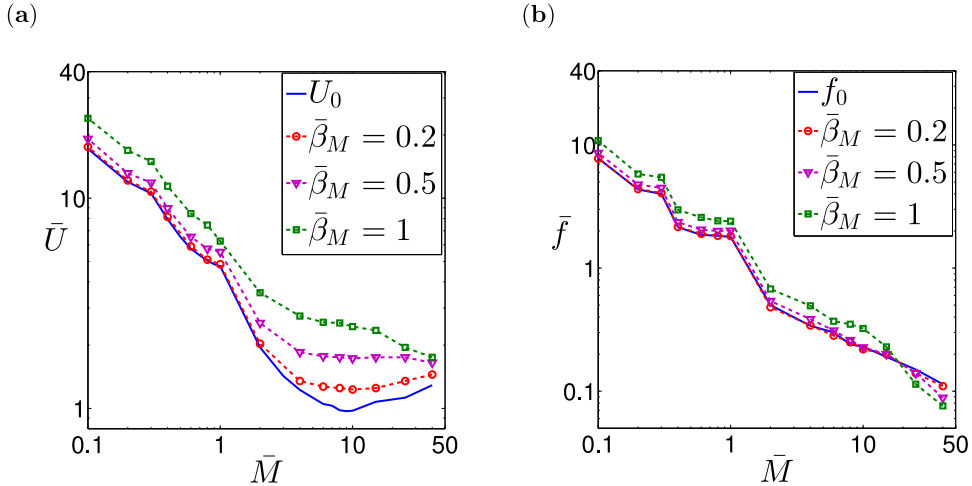


FIG. 4. Reduced flutter velocity (a) and frequency (b) results for fixed  $\bar{r} = 1$  and  $\bar{\beta}_M = 0.2, 0.5, 1$ . The flutter boundary results without piezoelectric effect are plotted with solid line.

at the flutter boundary. As the coupling factor  $\bar{\beta}_M$  increases, the vibration frequency increases as shown in Figure 4(b), due to the increase in effective stiffness by the piezoelectric material, which will be shown later when discussing the effect of the resistance.

A flapping flag without the piezoelectric effect transitions from a pre-flutter to a periodic flutter to a chaotic state as the incoming flow velocity increases<sup>16</sup> through a complicated process. Chen *et al.* identified five different periodic states and three chaotic states during the transition.<sup>51</sup> For simplicity, we only focus on the dynamic behavior of the flag near the flutter boundary, which corresponds to the first periodic state in the post-flutter region. In this region, previous work has shown that without the piezoelectric effect, the flapping frequency grows linearly with the inflow velocity and the amplitude also increases.<sup>9,11</sup> Since the piezoelectric material functions as a stabilizer to the system by increasing the bending stiffness, the flapping frequency and amplitude depend similarly on the incoming velocity near the flutter boundary with the piezoelectric effect. In the periodic state, we define the amount of the electric power generated in the circuit by a time and space averaged power over one period as  $P_R = \langle \frac{\bar{V}^2}{R} \rangle$ . The energy harvesting power depends on the voltage, which is related to the curvature (and hence the flapping amplitude) of the beam according to Equation (13). Therefore, power increases when the velocity increases. In Figure 5(a), we choose the power obtained right above the critical flutter speed  $\bar{U}$  as a representative to guarantee the flag is in the region of interest, with a fixed value of  $\bar{r} = 1$  for varying  $\bar{M}$  and  $\bar{\beta}_M$ .

In general, for the same mass ratio, the power increases with  $\bar{\beta}_M$  due to higher electro-mechanical coupling, i.e., more fluid kinetic energy is converted to electric energy. The power  $P_R$  scales as  $\bar{\beta}_M^2$  as shown in Figure 5(b), where we divide the power by  $\bar{\beta}_M^2$  and find a collapse of all the power curves. Equation (13) can be rewritten as  $\bar{V} = \bar{\beta}_M e^{-\frac{\bar{r}}{R}} \int e^{\frac{\bar{r}}{R}} \partial_{\bar{t}} \bar{\kappa} d\bar{t}$ . If we assume the curvature only weakly depends on the piezoelectric coupling factor, then  $\bar{V}$  scales with  $\bar{\beta}_M$  and the power scales with  $\bar{\beta}_M^2$ . As the mass ratio decreases, we obtain multiple peaks in  $P_R$ , and each of the peaks corresponds to a transition to a higher mode shape. A larger critical flutter speed is required when the flag changes to a higher mode shape, and the higher speed leads to more fluid kinetic energy converted to electrical energy, and hence larger power. The deviation in trend observed in Figure 5(a) for  $\bar{\beta}_M = 1$  at  $\bar{M} = 0.2$  and  $0.3$  is because the flag is still in the third mode shape for  $\bar{\beta}_M = 1$ , but changes to a fourth mode shape for  $\bar{\beta}_M = 0.2$  and  $0.5$ . Therefore, a higher energy is obtained at low  $\bar{\beta}_M$  values. In Figure 5(c), we show a diagram of different mode shapes obtained with various  $\bar{M}$  and  $\bar{\beta}_M$ . For the same mass ratio, the increasing  $\bar{\beta}_M$  increases the effective stiffness of the flag. Therefore, the flag oscillates in a lower mode shape, and the curve which differentiates different modes tends to lower mass ratios as  $\bar{\beta}_M$  increases.

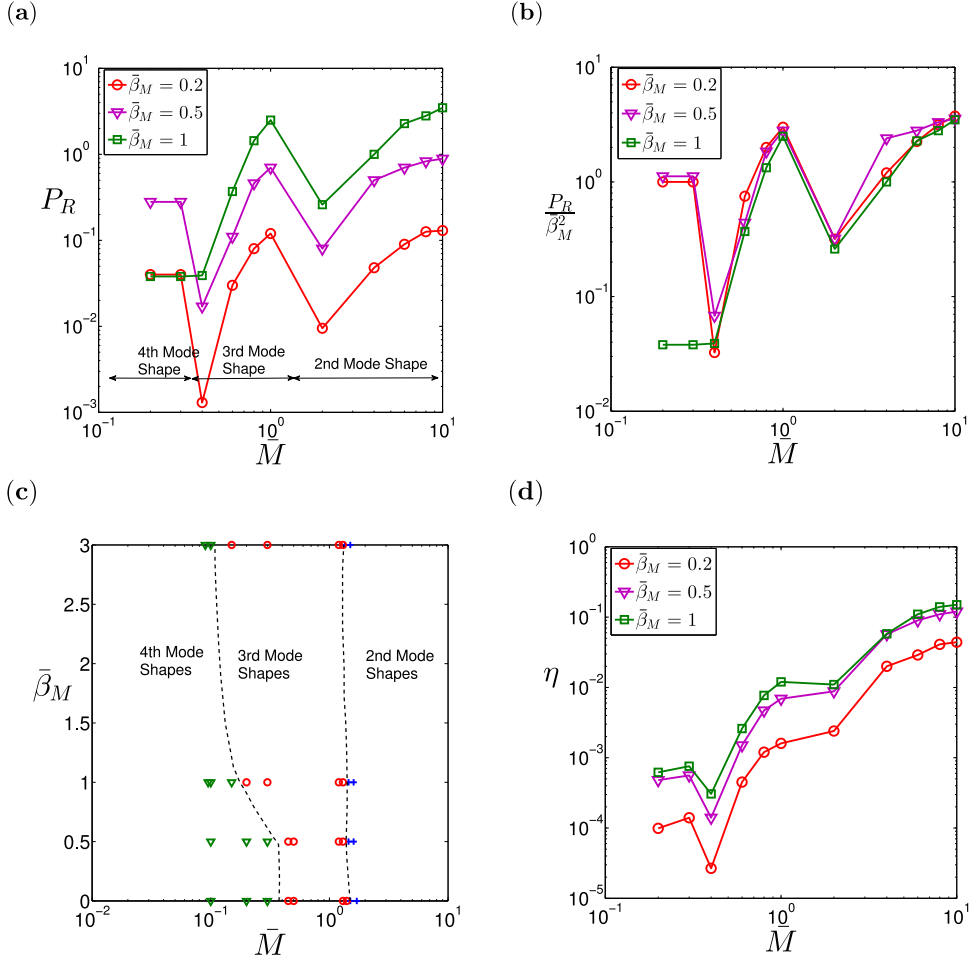


FIG. 5. (a) Averaged power  $P_R$  vs. mass ratio  $\bar{M}$  for fixed  $\bar{r} = 1$  and various  $\bar{\beta}_M = 0.2, 0.5, 1$ . (b) The averaged power obtained with different  $\bar{\beta}_M$  is rescaled by  $\bar{\beta}_M^2$  and a good collapse is obtained. (c) Diagram of mode shapes for different mass ratio  $\bar{M}$  and  $\bar{\beta}_M = 0, 0.5, 1, 3$ .  $\bar{\beta}_M = 0$  indicates the case without piezoelectric effect. (d) The averaged efficiency  $\eta$  vs.  $\bar{M}$  for fixed  $\bar{r} = 1$  and various  $\bar{\beta}_M = 0.2, 0.5, 1$ .

Similar to some previous work,<sup>19,28,52</sup> we consider the energy harvesting efficiency as the ratio of the output electric power to available fluid power,

$$\eta = \frac{\langle V^2/R \rangle}{\rho_f U^3 A S} = \frac{P_R}{\bar{U}^3 \bar{A}}, \quad (14)$$

where  $A$  and  $\bar{A}$  are the dimensional and dimensionless maximum vibration amplitude of the flag during one period. We show the corresponding efficiency obtained with the same parameters in Figure 5(d). In general, the efficiency decreases as  $\bar{M}$  decreases. Although the power increases when the mode shape changes, the flutter speed  $\bar{U}$  also increases. Therefore, the value of efficiency, which scales as  $\bar{U}^{-3} \bar{A}^{-1}$ , depends on the competition of the power, the incoming flow velocity, and the flapping amplitude, which in turn changes with  $\bar{M}$  as shown in Figure 5(d). Since the flapping amplitude  $\bar{A}$  will increase accordingly with the incoming velocity,  $\eta$  also decreases when the incoming velocity increases. Therefore, setting the incoming velocity to be right above the flutter velocity will improve the energy harvesting efficiency in the region of our interest.

Next, we consider the effect of the resistance on the flutter boundary. In Figure 6, we show the flutter boundary results for a fixed value of  $\bar{\beta}_M = 0.5$  and various  $\bar{r}$ . The dimensionless parameter  $\bar{r}$  is a property of the electric circuit. When  $\bar{r}$  is small, the circuit is close to a short circuit and the effect of piezoelectric material decreases. As shown in panel (a), the critical flutter velocities are

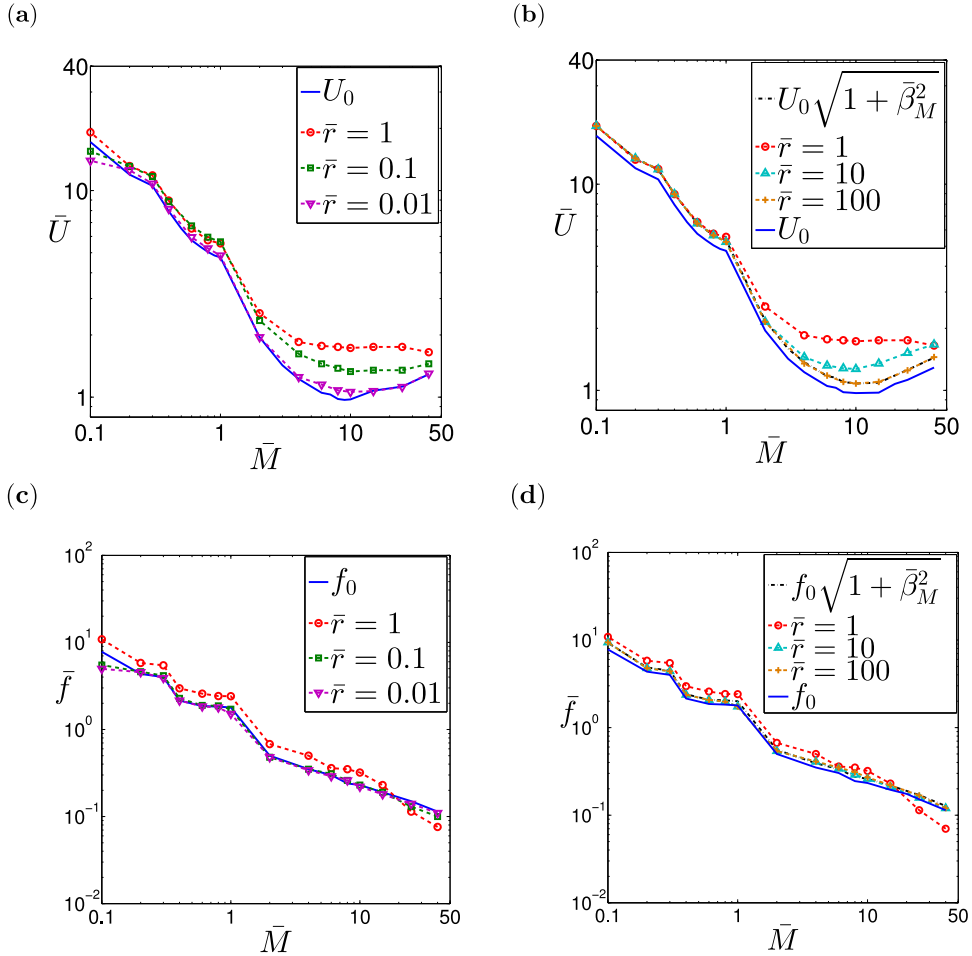


FIG. 6. (a) Critical flutter speed for fixed  $\bar{\beta}_M = 0.5$  and  $\bar{r} = 0.01, 0.1, 1$ . The flutter speed without piezoelectric effect is  $U_0$  plotted with solid line. (b) Critical flutter speed for fixed  $\bar{\beta}_M = 0.5$  and  $\bar{r} = 1, 10, 100$ . Solid line shows  $U_0$  and dashed-dotted line shows the curve  $U_0(1 + \bar{\beta}_M^2)^{1/2}$ . (c) Frequency values at the flutter boundary for fixed  $\bar{\beta}_M = 0.5$  and  $\bar{r} = 0.01, 0.1, 1$ . The frequency without piezoelectric effect  $f_0$  is plotted with solid line. (d) Frequency values at the flutter boundary for fixed  $\bar{\beta}_M = 0.5$  and  $\bar{r} = 1, 10, 100$ . Solid line shows  $f_0$  and dashed-dotted line shows the curve  $f_0(1 + \bar{\beta}_M^2)^{1/2}$ .

closer to  $U_0$  as  $\bar{r} \rightarrow 0$ . When  $\bar{r}$  is large, the circuit is close to an open circuit. In the limiting case when  $\bar{r} \rightarrow \infty$ , the circuit equation can be rewritten as

$$\bar{V} = -\bar{\beta}_M \bar{\kappa}, \quad (15)$$

therefore, the flag behaves equivalently to a flexible flag with a higher bending rigidity of  $B(1 + \bar{\beta}_M^2)$  and the critical velocity should be  $U_0(1 + \bar{\beta}_M^2)^{1/2}$ . When the resistance has a moderate value, the voltage does not depend linearly on the curvature. However, it can still be represented by the product of  $\bar{\beta}_M$  and a function of curvature, which suggests an increase in the system's bending stiffness with an increasing  $\bar{\beta}_M$ . We notice that this observation is consistent with the results obtained by Doaré and Michelin.<sup>24</sup> In Figure 6(b), we plot the stability boundary results for fixed  $\bar{\beta}_M = 0.5$  and  $\bar{r} = 1, 10, 100$  together with the curve  $U_0(1 + \bar{\beta}_M^2)^{1/2}$  and  $U_0$ , and we can see that when  $\bar{r} = 100$ , the curve approaches the curve  $U_0(1 + \bar{\beta}_M^2)^{1/2}$ . The corresponding vibration frequencies for varying  $\bar{r}$  are shown in panels (c) and (d) of Figure 4. Similarly to the critical speed, when  $\bar{r} \rightarrow 0$ , the frequency tends to  $f_0$ ; when  $\bar{r} \rightarrow \infty$ , the frequency tends to  $f_0(1 + \bar{\beta}_M^2)^{1/2}$ .

Another important observation from Figures 4 and 6 is that the numerical results show that the increase in flutter velocity by PZT (with increase in  $\bar{\beta}_M$  and  $\bar{r}$ ) is more rapid for cases with higher

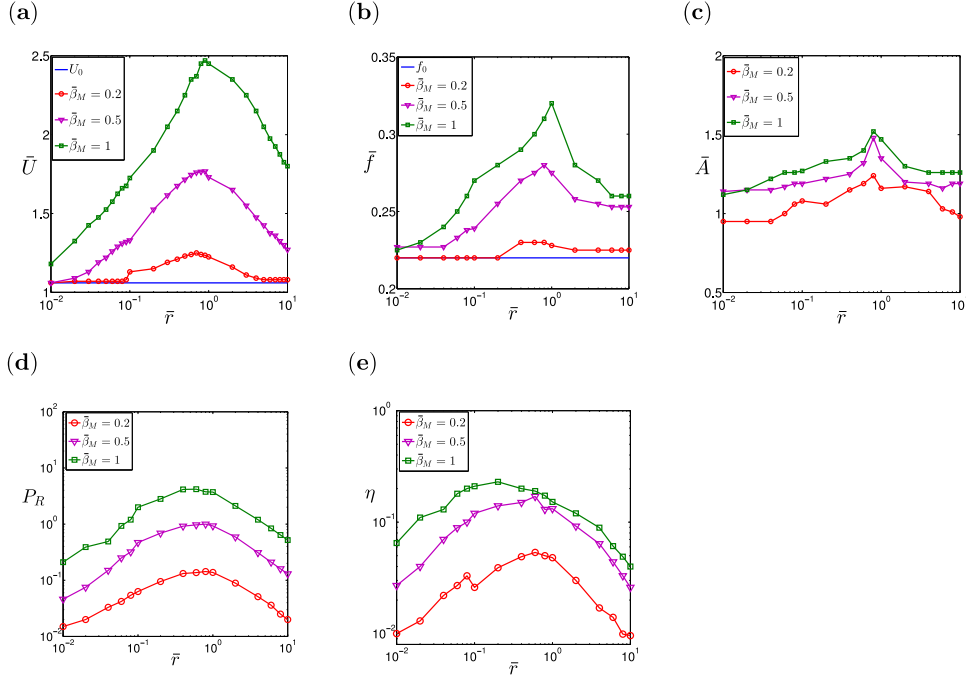


FIG. 7. (a) Flutter velocity  $\bar{U}$  vs. resistance  $\bar{r}$ . The solid line without symbols denotes  $U_0$ , the flutter velocity when no piezoelectric material is included. (b) Vibration frequency right above the flutter boundary  $\bar{f}$  vs. resistance  $\bar{r}$ . The solid line without symbols denotes  $f_0$ , the frequency when no piezoelectric material is included. (c) Flapping amplitude  $\bar{A}$  vs.  $\bar{r}$ . (d) Averaged power  $P_R$  vs.  $\bar{r}$ . (e) Averaged efficiency  $\eta$  vs.  $\bar{r}$ . Other parameters used for three panels are  $\bar{M} = 10$ ,  $\bar{\beta}_M = 0.2, 0.5, 1$ .

$\bar{M}$  ( $\bar{M} > 1$ ), i.e., heavier flags in a lighter fluid. When the mass ratio is small, the fluid inertia will dominate the system and the piezoelectric material will have a relatively negligible impact on the beam vibrational response.

Unlike the trend with varying  $\bar{\beta}_M$ , the flutter velocity as well as the flutter frequency change non-monotonically with  $\bar{r}$ , as shown in Figure 6. In Figure 7, we plot the flutter velocity, the corresponding vibration frequency, the flapping amplitude, the averaged electric power, and efficiency right above the flutter boundary varying over a range of  $\bar{r}$  with a fixed mass ratio  $\bar{M} = 10$  and  $\bar{\beta}_M = 0.2, 0.5, 1$ . We also plot  $U_0$  and  $f_0$  with solid lines for comparison.

For all three  $\bar{\beta}_M$  values, the nondimensional resistance which leads to largest flutter speed is obtained around  $\bar{r} = 1$ , when the fluid kinetic energy is balanced by the energy dissipated in the resistor and stored as electric energy in the piezoelectric material. The maximum flutter frequency, the flapping amplitude, and averaged electric power are also achieved at these intermediate points. Since the efficiency scales as  $\bar{U}^{-3}\bar{A}^{-1}$ , the largest  $\eta$  is obtained at a smaller value of  $\bar{r}$  as shown in panel (e). The existence of an optimal resistance load was studied previously for piezoelectric beams in a vacuum with base excitations,<sup>35,36</sup> and was also observed for piezoelectric beams in viscous flow.<sup>19</sup>

## 2. Piezoelectric effect with inductance

Now we consider the effects of inductance on the flutter boundary. Similarly to the effect of the resistance, when inductance tends to zero and the circuit frequency tends to infinity ( $f_e \rightarrow \infty$ ), the circuit tends to a short circuit and the effect of the piezoelectric material is negligible. When inductance tends to infinity and the circuit frequency tends to zero ( $f_e \rightarrow 0$ ), the circuit tends to an open circuit and the circuit is a purely resistive circuit as discussed in Sec. III B 1.

When the inductance has a moderate value, we find that the piezoelectric flag always exhibits a chaotic motion in the post-flutter regime. Periodic solutions with small perturbations are found

close to the flutter boundary when  $\bar{\beta}_M < 1$ . Therefore, instead of considering the power and efficiency over one period, we use an averaged power  $P_R$  and efficiency  $\eta$  over a long time in the large-amplitude regime as measurements. In Figure 8, we show the critical flutter speed, vibration frequency, and the corresponding averaged power and efficiency over a range of the circuit frequency  $f_e$  with fixed mass ratio  $\bar{M} = 1$ ,  $\bar{\tau} = 1$  and various  $\bar{\beta}_M = 0.2, 0.5, 0.8$ .

In panel (a) of Figure 8, we notice a drop in the critical flutter speed as the circuit frequency  $f_e$  increases above a certain value. The flag is able to flutter at a much lower speed due to the “lock-in” between the circuit resonant frequency and the flag resonant frequency, i.e.,  $\bar{f} = f_e$ . In panel (b), we plot the vibration frequency  $\bar{f}$  and the circuit frequency  $f_e$  together with a solid line to denote the resonance situation where  $\bar{f} = f_e$ . We note that since the flag undergoes chaotic motion in this state, the oscillation frequency of the flag is not single-valued. We instead use the peak of the power spectrum of the frequency in the large-amplitude flapping state. Therefore, we observe some discrepancies between the flag vibration frequency and the circuit resonant frequency. Nonetheless, in a certain range of  $f_e$ , the slope of the two frequency curves matches well with each other, and the flutter speed decreases rapidly in the “lock-in” range. This “lock-in” phenomenon was also observed by Xia *et al.*,<sup>28</sup> and they also noticed a sudden decrease in the flutter speed with a slender

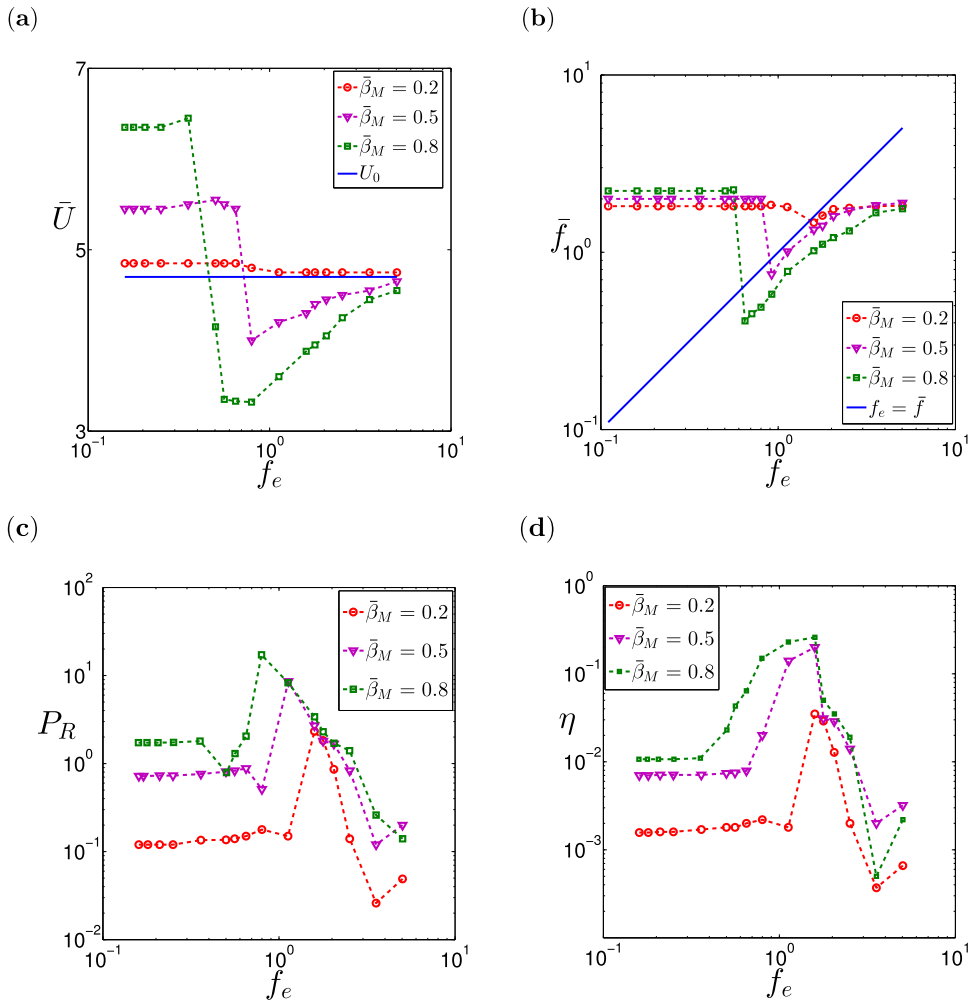


FIG. 8. Flutter boundary results for  $\bar{M} = 1$ ,  $\bar{\tau} = 1$ , and  $\bar{\beta}_M = 0.2, 0.5, 0.8$ . (a) Critical flutter speed  $\bar{U}$  vs. circuit frequency  $f_e$ . The solid line indicates the flutter speed  $U_0$  when no piezoelectric material is included. (b) Vibration frequency  $\bar{f}$  vs. circuit frequency  $f_e$ . The solid line shows the line when  $\bar{f} = f_e$ , which corresponds to the “lock-in” situation. (c) Averaged power dissipated on the resistance  $P_R$  vs.  $f_e$ . (d) Averaged efficiency  $\eta$  vs.  $f_e$ .

body model. In the “lock-in” regime, we notice a rapid increase in the power dissipated in the resistor, as well as the efficiency, as shown in panels (c) and (d). This is an important improvement for an energy harvester, since one of the limitations of self-sustained energy harvesters is their requirement for flow speed which is difficult to achieve in a natural environment. By tuning the inductance into the “lock-in” regime, the energy harvester is able to flutter at a much lower speed and produce a much higher energy. We also note that as  $\bar{\beta}_M$  increases and the piezoelectric coupling becomes larger, the flutter velocity can be reduced to a lower value, as shown in panel (a), and the frequency lock-in regime is larger, as shown in panel (b).

The flutter speed is greatly reduced in the “lock-in” regime as the flag jumps to a lower mode shape which requires less fluid kinetic energy to initiate flutter. If the flag is already in the lowest mode shape (second mode shape) and cannot be reduced further (such as for  $\bar{M} > 2$  according to Figure 2(a)), we find that the flutter speed will not be reduced even though vibration frequency can still match the circuit frequency. In Figure 9, we show the flutter speed, the corresponding vibration frequency, the energy harvesting power, and efficiency over a range of circuit resonant frequencies with fixed values of  $\bar{\beta}_M$  and  $\bar{F}$  and different mass ratios. In Figure 10, we show the snapshots of the flag at different mass ratios with and without the inductor. The values of  $f_e$  are chosen so that the vibration frequency of the beam is “lock-in” to the circuit resonant frequency.

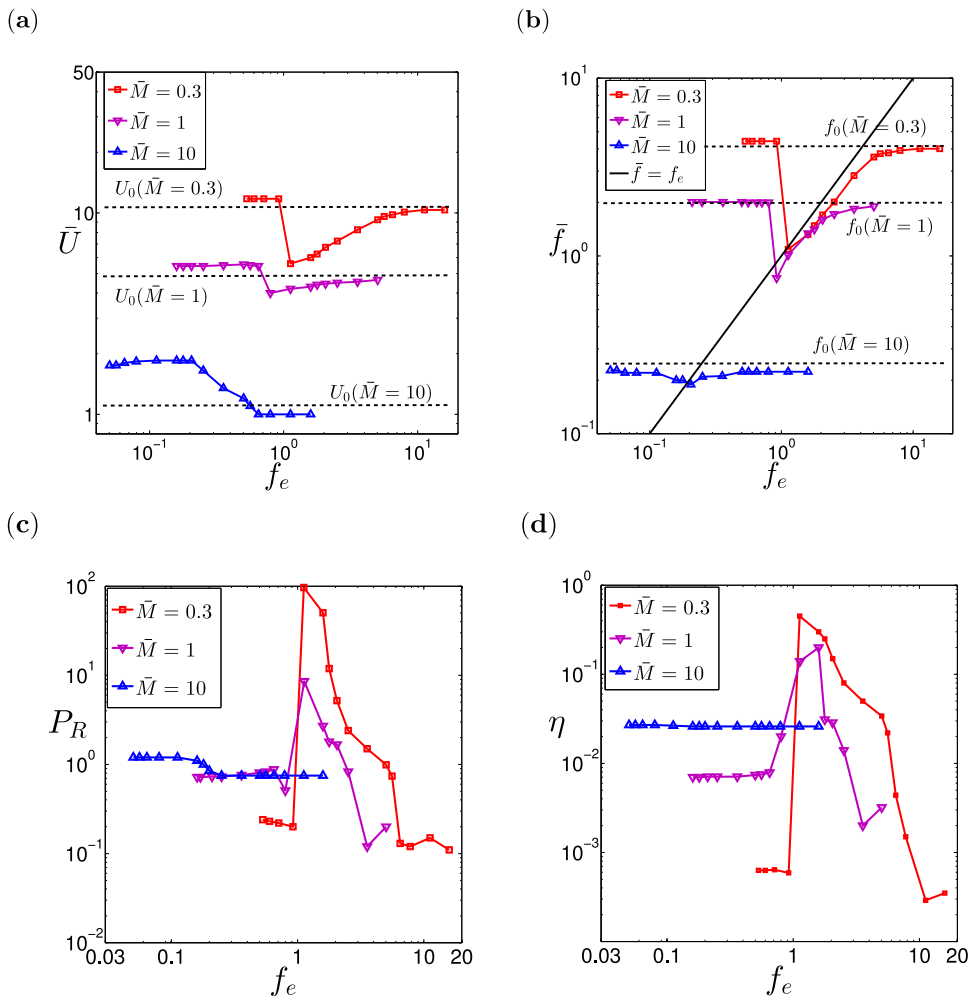


FIG. 9. (a) Flutter speed  $\bar{U}$  vs.  $f_e$ , (b) vibration frequency  $\bar{f}$  vs.  $f_e$ , (c) power  $P_R$  vs.  $f_e$ , (d) efficiency  $\eta$  vs.  $f_e$  at  $\bar{M} = 0.3, 1, 10$ ,  $\bar{\beta}_M = 0.5$ , and  $\bar{F} = 1$ . Dashed lines denote the flutter speeds and frequency without piezoelectric effect for different mass ratios. Solid line in panel (b) denotes the curve  $\bar{f} = f_e$ .

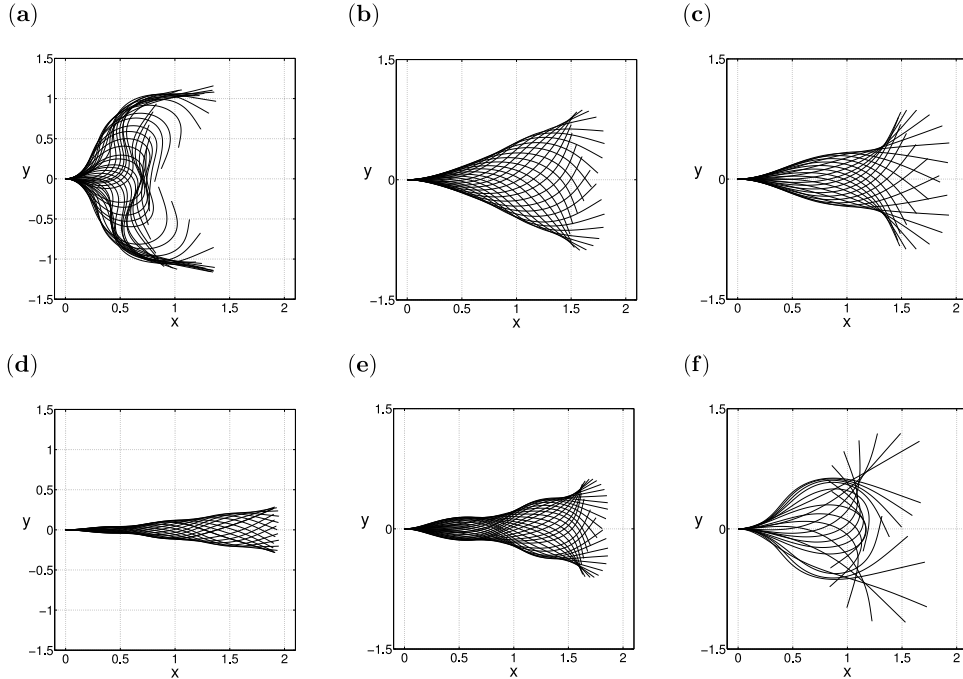


FIG. 10. Flag snapshots at different  $\bar{M}$  and fixed values of  $\bar{\beta}_M = 0.5$  and  $\bar{r} = 1$ , with the inductor (a)-(c) at “lock-in”  $\bar{f} = f_e$ , and without the inductor (d)-(f). (a) Second mode shape,  $\bar{M} = 0.3$ ,  $\bar{U} = 5.7$ , and  $f_e = 1$ . (b) Second mode shape,  $\bar{M} = 1$ ,  $\bar{U} = 4.2$ , and  $f_e = 0.9$ . (c) Second mode shape,  $\bar{M} = 10$ ,  $\bar{U} = 1.9$ , and  $f_e = 0.2$ . (d) Fourth mode shape,  $\bar{M} = 0.3$  and  $\bar{U} = 10.9$ . (e) Third mode shape,  $\bar{M} = 1$  and  $\bar{U} = 5.6$ . (f) Second mode shape,  $\bar{M} = 10$  and  $\bar{U} = 1.9$ .

Without the inductor, the flag flutters in the 4th and 3rd modes, respectively, for  $\bar{M} = 0.3$  and 1, as shown in Figures 10(d) and 10(e). However, in the “lock-in” regime, the flag flutters in the 2nd mode for both cases as shown in panel (a) and (b). When  $f_e$  is small, the circuit is close to a purely resistive circuit, and the flutter speed and vibration frequency with the PZT are larger than  $U_0$  and  $f_0$ . Notice in Figure 4(a), the piezoelectric material is more effective for larger  $\bar{M}$  ( $\bar{M} > 1$ ) at  $\bar{\beta}_M = 0.5$ . Therefore, the flutter velocity  $\bar{U}$  increases more for  $\bar{M} = 10$  than the other two cases. As  $f_e$  increases and approaches the lower bound of “lock-in” regime, the flutter speed and vibration frequency of the flag drop rapidly at first; as  $f_e$  continues increasing, the flutter speed and vibration frequency gradually increase, eventually back to  $U_0$  and  $f_0$ , as  $f_e \rightarrow \infty$  corresponds to the short circuit scenario. When  $\bar{M} = 10$ , although the two frequencies still match each other around  $f_e = 0.2$ , the flutter velocity simply decreases to  $U_0$  as  $f_e$  increases. In Figures 10(c) and 10(f) for  $\bar{M} = 10$ , the flag flutters in the 2nd mode with/without the inductor, although the motions are different. In addition, notice in Figure 9 that the “lock-in” range is wider for lower  $\bar{M}$ , where there is more room for the vibrating flag to drop down to the lowest flutter mode (2nd mode). Without the inductance, we have shown that the energy harvesting power and efficiency are larger for  $\bar{M} = 10$  compared to those of  $\bar{M} = 1$  and 0.3, as shown in Figures 5(a) and 5(d). However, with the resonant circuit, the power and efficiency for smaller mass ratios are both greatly improved when in the lock-in regime, and become even larger than those of  $\bar{M} = 10$ . This indicates that when the fluid is light or the solid is heavy ( $\bar{M} > 1$ ), the RL shunting circuit is not effective at modifying the flutter velocity or frequency. On the other hand, the results indicate that the RL shunting circuit can be used to tune the vibration responses of a lightweight piezoelectric flag in a heavy fluid such as water ( $\bar{M} \leq 1$ ).

#### IV. SCALABILITY OF PIEZOELECTRIC BEAMS

Now, we consider several commonly used commercial materials and show how to apply the above discussion to actual devices in different fluids. We first show some typical values of the above

dimensionless parameters for PZT plates in air and water. We consider a rectangular plate with chord length of 0.05 m, a thickness-to-chord ratio of 0.2%, and a span-to-chord ratio of 1. These are typical dimensions for a thin plate and are similar to some of the experimental systems.<sup>9,11,35</sup> PZT-5H is selected to be the piezoelectric material due to its high piezoelectric coupling coefficient relative to other PZT materials. Each PZT patch is assumed to have a fixed thickness  $q_p$  of 0.02 mm, and the substrate material has a fixed thickness  $q_s$  of 0.06 mm. The dimensional piezoelectric coupling coefficient is then  $6.6 \times 10^{-5}$  m N/V, and the internal capacitance is  $6.4 \times 10^{-6}$  F for each patch. The loaded resistance is chosen to be 1 k $\Omega$  and the inductance is 0.1 H.

In Table II, we list the density, Young's modulus, and Poisson's ratio for four common substrate materials (Balsa Wood, Polymer (POM), aluminum alloy, and steel) spanning a wide range of material density and elasticity values. We also list the material properties of the PZT-5H. The bending rigidity for the composite piezoelectric flag is calculated by

$$B = EI = \frac{E_s}{1 - \nu_s^2} \frac{q_s^3 S}{12} + \frac{E_p}{1 - \nu_p^2} S \left( \frac{1}{2} q_s^2 q_p + q_s q_p^2 + \frac{2}{3} q_p^3 \right), \quad (16)$$

where  $E_s, \nu_s$  and  $E_p, \nu_p$  are the Young's modulus and Poisson's ratio for the substrate and the PZT patch, respectively. In Figure 11, we show the dimensionless  $\bar{M}$ ,  $\bar{\beta}_M \bar{r}$ , and  $f_e$  for different materials according to the definitions given in Table I.

We consider two types of fluids: air and water to cover the range of  $\bar{M}$ , i.e., heavy flags in light fluid and light flags in heavy fluid, respectively.

First, we note that  $\bar{\beta}_M$  is unchanged as the fluid medium changes from air to water since it is not a function of  $\rho_f$ , as shown in Table I. Notice from Table II, the PZT patch has a large density and Young's modulus compared to many substrate materials. In general, the mass ratio of various flags in water is much smaller than those in air,  $\bar{M}$  is around 10–30 for flags in air, and therefore they mainly flutter in the second mode. For flags in water,  $\bar{M}$  is around 0.01–0.03; they flutter in a higher mode and the critical flutter speed without PZT is much larger, as shown in Figure 2.

TABLE II. Parameters of the solid material and PZT-5H.

	Balsa wood	POM	Alumina alloy	Steel	PZT-5H
Density $\rho$ (kg/m <sup>3</sup> )	97.1	1480	2800	7850	7700
Young's modulus $E$ (GPa)	1.8	3	79	210	66
Poisson's ratio	0.36	0.35	0.33	0.3	0.34

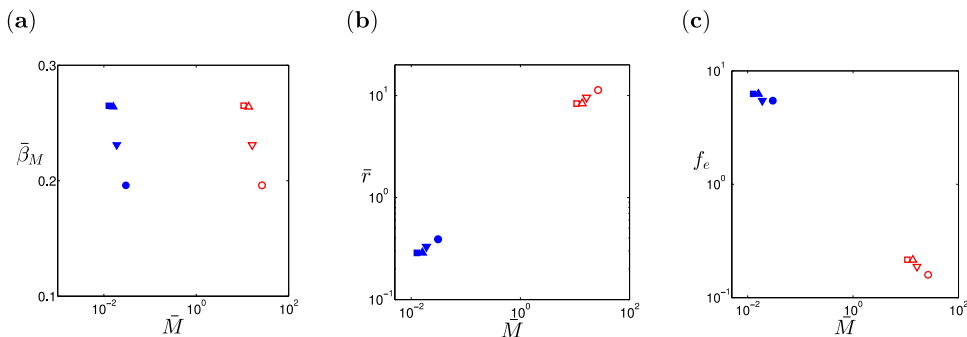


FIG. 11. Range of dimensionless parameters corresponding to different materials. The open symbols indicate materials in air, and the filled symbols indicate materials in water.  $\circ/\nabla/\triangle/\square$ : steel/aluminum alloy/POM/Balsa wood in air;  $\bullet/\blacktriangledown/\blacktriangle/\blacksquare$ : steel/Aluminum alloy/POM/balsa wood in water. (a)  $\bar{M}$  vs.  $\bar{\beta}_M$ , (b)  $\bar{M}$  vs.  $\bar{r}$ , (c)  $\bar{M}$  vs  $f_e$ .

TABLE III. The effect of the PZT on the flutter speed, frequency, power, and efficiency for a POM flag in air and water.

Fluid	Air ( $\rho_f = 1.18 \text{ kg/m}^3$ ) $\bar{M} = 13.6, \bar{\beta}_M = 0.26$			Water ( $\rho_f = 998 \text{ kg/m}^3$ ) $\bar{M} = 0.016, \bar{\beta}_M = 0.26$		
	No PZT	R 1000 $\Omega$	Optimal R 127 $\Omega$	No PZT	R 1000 $\Omega$	Optimal R 3477 $\Omega$
Resistance only						
Circuit						
Flutter speed (m/s)	14.9	20	22.4	18	18.2	18.4
Frequency (Hz)	131	137	118	323	150	150
Power $P_R$ (W)	...	0.67	3.55	...	0.93	0.27
Efficiency $\eta$	...	0.023	0.078	...	$3.4 \times 10^{-4}$	$1.0 \times 10^{-4}$
RL circuit						
	No PZT	L 0.1 H	No optimal L	No PZT	L 0.1 H	Optimal L 0.93 H
Flutter speed (m/s)	14.9	14.9	...	18	8.7	4.9
Frequency (Hz)	131	131	...	323	44	13
Power $P_R$ (W)	...	0.32	...	...	1.78	3.1
Efficiency $\eta$	...	0.0015	...	...	0.02	0.14

The dimensionless resistance density  $\bar{r}$  decreases and the circuit frequency  $f_e$  increases substantially when the fluid becomes heavier as shown in panels (b) and (c) of Figure 11, respectively. We also note that the dimensionless  $\bar{r}$  and  $f_e$  depend on the values of resistance and inductance, and therefore can be easily adjusted by changing their values.

Now, we take POM as an example and show the dimensional flutter speed, vibration frequency, averaged power, and efficiency in air and water under different conditions in Table III. We consider both the resistance only circuit and the RL circuit. The effectiveness of the resistance only circuit on modifying the flutter speed and frequency is larger for flags in air, and practically negligible for flags in water. By using the optimal resistance value in a resistance only circuit shown in Table III, the flutter speed is increased by 50% compared to the case without PZT when the flag is placed in air, but only by 2% when it is placed in water. A larger electric power and efficiency are also obtained with the optimal R when the flag is placed in air. For heavy fluids, the optimal R value which leads to a larger flutter velocity results in a smaller power and efficiency. The voltages for different R values are almost identical in this case, so the power and efficiency decrease with a higher resistance.

On the other hand, for a RL shunting circuit, the flag in the lighter fluid mainly flutters in the second mode (the lowest flutter mode), and hence the flutter speed and the frequency will not be greatly reduced by the inductance, and there is not an optimal inductance value. The RL circuit is more effective for lighter flags in a heavier fluid, as shown in the example of water in Table III. We consider the RL circuit with the optimal R value. When the flag is placed in water, by tuning the inductor to the “lock-in” range, the flutter speed is reduced by 75% compared to the case without PZT. The averaged power increased by a factor of 10 compared to the case with a purely resistive circuit and the efficiency increased by a factor of 1000. Note that both circuits have important practical applications. An increase of the flutter speed is typically desired for vibration control applications, while a decrease is typically desired for energy harvesting applications.

For an actual device with a larger size and complete geometric similarities, i.e., if the thickness-to-chord ratio, thickness ratio of the PZT patch to substrate material, and span-to-chord ratio are fixed, then the dimensionless  $\bar{M}$ ,  $\bar{\beta}_M$ , and  $\bar{r}$  are unchanged with the length scale for the same PZT and substrate material, fluid and resistance values. According to Table I,  $\bar{\beta}_M = \beta_M \sqrt{\frac{1}{Bc_p}}$ . If we assume the length scale is  $b$ , then the dimensional  $\beta_M$  scales as  $b^2$ ,  $B$  scales as  $b^4$ , and capacitance density is unchanged with the length, which implies that  $\bar{\beta}_M$  is unchanged with the length scale. A similar analysis shows that  $\bar{r}$  is also invariant with the length.  $f_e$  is proportional to  $b^{-1/2}$ , but when the length increases, the same dimensionless value can be obtained by changing the value of the inductor. Therefore, the dimensionless results obtained from the model problems can be

directly applied to the full scale problems. The dimensional velocity is invariant with respect to  $b$ , the frequency scales as  $b^{-1}$  and the power scales as  $b^2$ . Therefore, when the problem is extended to a larger size, the flutter speed is unchanged, but a smaller frequency and a larger power are expected.

On the other hand, the actual thickness of the PZT patch cannot exceed several centimeters due to material properties and manufacture restrictions. Thus, the thickness ratio of the PZT patch and the substrate material can be much smaller than that of the model scale problem, which leads to a smaller  $\bar{\beta}_M$ . Another important issue is that the thickness to chord ratio is generally larger for an actual device, otherwise the plate may undergo material failure, which is not considered in the current analysis. The bending rigidity  $B$  is larger for a thicker plate, and it leads to a larger flutter speed which scales as  $B^{1/2}$  according to Table I. Moreover, although the substrate material can be scaled, the material properties of the PZT patch can be difficult to scale. For example, very large PZT patches are generally not feasible in reality, so several discrete patches are often linked together as an alternative. These issues along with the stability of the particular material in a certain fluid must be considered when extending the model scale results to full scale problems.

## V. CONCLUSIONS

In this work, we investigate the effect of the PZT material on the flutter velocity, vibration mode and frequency, and energy harvesting power and efficiency of a flexible flag in different fluid medium. We develop a fully coupled fluid-solid-electric model by combining the inviscid vortex sheet model with a linear electro-mechanical coupling model. A cantilever flag with two layers of PZT and a uniform inflow is studied as a model problem. Based on a nondimensional analysis, four dimensionless parameters  $\bar{M}, \bar{\beta}_M, \bar{r}, f_e$  were found to govern the reduced flutter velocity  $\bar{U}$  and frequency  $\bar{f}$  of the piezoelectric flag.

When the mass ratio  $\bar{M}$  is small, the flag flutters at higher mode, as the relative high fluid inertia and fluid disturbing force allow higher wavenumber deforming patterns. Flags with lower  $\bar{M}$  also require a larger inflow velocity to initiate flutter, due to the higher relative fluid inertia and the damping resistance against motion.

Two types of output circuits are considered in this work: a purely resistive circuit and a resonant RL circuit. For a purely resistive shunting circuit, the PZT material functions as a stabilizer to the system by increasing the effective system stiffness and damping. Therefore, as  $\bar{\beta}_M$  increases, the flutter speed, as well as the vibration frequency, averaged power and efficiency also increase. In particular, we find that the power scales as  $\bar{\beta}_M^2$ . For a resistance only circuit, the optimal resistance to maximize the flutter speed and the power is obtained at near  $\bar{r} = 1$ , when the fluid kinetic energy is balanced by the energy dissipated in the resistor and stored as electrical energy in the piezoelectric material. The results also show that a purely resistive circuit has a greater impact for heavier flags in lighter fluids, i.e.,  $\bar{M} > 1$ . For  $\bar{M} \ll 1$ , the PZT flag with a resistance only circuit has a negligible impact if  $\bar{\beta}_M < 0.2$  and/or  $\bar{r} < 0.1$ , which is the case for most PZT flags in water. For a resonant RL circuit, an optimal inductor is found when the circuit frequency matches the flag's vibration frequency. In this "lock-in" regime, the flutter speed and frequency are greatly reduced and the flag will flutter in a lower mode. The "lock-in" range is found to be larger, and the flutter speed and the vibration frequency drop more in this range for lower  $\bar{M}$ . Maxima electric power and efficiency are also obtained in the "lock-in" regime.

We also consider a model scale setup with several commonly used commercial materials in air and water. Typical ranges of dimensionless parameters are obtained for four types of materials that span a wide range of solid density and rigidity values. For POM, we find that the resistance only circuit is more effective when the flag is placed in a lighter fluid like air. A RL circuit is able to significantly reduce the flutter speed and frequency when the flag is placed in a heavier fluid like water, but is not as effective for similar flags in air. For vibration control applications, an increase in the flutter speed is typically desired. On the other hand, for energy harvesting applications, a lower flutter speed is desired.

An extension of this work is to consider the application of the PZT material on passive vibration control and for energy harvesting with a vibrating foil, which requires generalizing the current vortex sheet model to more complicated geometric shapes, and considering a combined bending

and twisting deformation. Moreover, the influence of viscous and 3-D effects on electro-fluid-solid interactions requires additional study.

## ACKNOWLEDGMENTS

We acknowledge support from a Sloan Research Fellowship and NSF-DMS No. 1329726 (S.A.). We are also grateful for the funding provided by Office of Naval Research (ONR) Grant No. N00014-13-0383, managed by Dr. Ki-Han Kim.

- <sup>1</sup> S. R. Anton and H. A. Sodano, "A review of power harvesting using piezoelectric materials (2003–2006)," *Smart Mater. Struct.* **16**(3), R1 (2007).
- <sup>2</sup> K. A. Cook-Chennault, N. Thambi, and A. M. Sastry, "Powering mems portable devices: A review of non-regenerative and regenerative power supply systems with special emphasis on piezoelectric energy harvesting systems," *Smart Mater. Struct.* **17**(4), 043001 (2008).
- <sup>3</sup> N. W. Hagood and A. von Flotow, "Damping of structural vibrations with piezoelectric materials and passive electrical networks," *J. Sound Vib.* **146**(2), 243–268 (1991).
- <sup>4</sup> S. Behrens, A. J. Fleming, and S. O. R. Moheimani, "A broadband controller for shunt piezoelectric damping of structural vibration," *Smart Mater. Struct.* **12**(1), 18 (2003).
- <sup>5</sup> L. R. Corr and W. W. Clark, "Comparison of low-frequency piezoelectric switching shunt techniques for structural damping," *Smart Mater. Struct.* **11**(3), 370 (2002).
- <sup>6</sup> S. Taneda, "Waving motions of flags," *J. Phys. Soc. Jpn.* **24**(2), 392–401 (1968).
- <sup>7</sup> L. Huang, "Flutter of cantilevered plates in axial flow," *J. Fluids Struct.* **9**(2), 127–147 (1995).
- <sup>8</sup> J. Zhang, S. Childress, A. Libchaber, and M. Shelley, "Flexible filaments in a flowing soap film as a model for one-dimensional flags in a two-dimensional wind," *Nature* **408**(6814), 835–839 (2000).
- <sup>9</sup> Y. Watanabe, S. Suzuki, M. Sugihara, and Y. Sueoka, "An experimental study of paper flutter," *J. Fluids Struct.* **16**(4), 529–542 (2002).
- <sup>10</sup> D. M. Tang, H. Yamamoto, and E. H. Dowell, "Flutter and limit cycle oscillations of two-dimensional panels in three-dimensional axial flow," *J. Fluids Struct.* **17**(2), 225–242 (2003).
- <sup>11</sup> M. Shelley, N. Vandenbergh, and J. Zhang, "Heavy flags undergo spontaneous oscillations in flowing water," *Phys. Rev. Lett.* **94**(9), 094302 (2005).
- <sup>12</sup> C. Q. Guo and M. P. Paidoussis, "Stability of rectangular plates with free side-edges in two-dimensional inviscid channel flow," *J. Appl. Mech.* **67**(1), 171–176 (2000).
- <sup>13</sup> L. Zhu and C. S. Peskin, "Simulation of a flapping flexible filament in a flowing soap film by the immersed boundary method," *J. Comput. Phys.* **179**(2), 452–468 (2002).
- <sup>14</sup> M. Argentina and L. Mahadevan, "Fluid-flow-induced flutter of a flag," *Proc. Natl. Acad. Sci. U. S. A.* **102**(6), 1829–1834 (2005).
- <sup>15</sup> B. S. H. Connell and D. K. P. Yue, "Flapping dynamics of a flag in a uniform stream," *J. Fluid Mech.* **581**, 33–67 (2007).
- <sup>16</sup> S. Alben and M. J. Shelley, "Flapping states of a flag in an inviscid fluid: Bistability and the transition to chaos," *Phys. Rev. Lett.* **100**(7), 074301 (2008).
- <sup>17</sup> L. Tang and M. P. Paidoussis, "On the instability and the post-critical behaviour of two-dimensional cantilevered flexible plates in axial flow," *J. Sound Vib.* **305**(1), 97–115 (2007).
- <sup>18</sup> S. Michelin, S. G. Llewellyn Smith, and B. J. Glover, "Vortex shedding model of a flapping flag," *J. Fluid Mech.* **617**, 1–10 (2008).
- <sup>19</sup> D. T. Akcabay and Y. L. Young, "Hydroelastic response and energy harvesting potential of flexible piezoelectric beams in viscous flow," *Phys. Fluids* **24**(5), 054106 (2012).
- <sup>20</sup> Y. Watanabe, K. Isogai, S. Suzuki, and M. Sugihara, "A theoretical study of paper flutter," *J. Fluids Struct.* **16**(4), 543–560 (2002).
- <sup>21</sup> C. Eloy, C. Souilliez, and L. Schouveiler, "Flutter of a rectangular plate," *J. Fluids Struct.* **23**(6), 904–919 (2007).
- <sup>22</sup> M. J. Patil, D. H. Hodges, and C. E. S. Cesnik, "Limit-cycle oscillations in high-aspect-ratio wings," *J. Fluids Struct.* **15**(1), 107–132 (2001).
- <sup>23</sup> E. Virost, X. Amandolese, and P. Hémon, "Fluttering flags: An experimental study of fluid forces," *J. Fluids Struct.* **43**, 385–401 (2013).
- <sup>24</sup> O. Doaré and S. Michelin, "Piezoelectric coupling in energy-harvesting fluttering flexible plates: linear stability analysis and conversion efficiency," *J. Fluids Struct.* **27**(8), 1357–1375 (2011).
- <sup>25</sup> G. K. Ottman, H. F. Hofmann, A. C. Bhatt, and G. A. Lesieutre, "Adaptive piezoelectric energy harvesting circuit for wireless remote power supply," *IEEE Trans. Power Electron.* **17**(5), 669–676 (2002).
- <sup>26</sup> M. J. Guan and W. H. Liao, "On the efficiencies of piezoelectric energy harvesting circuits towards storage device voltages," *Smart Mater. Struct.* **16**(2), 498 (2007).
- <sup>27</sup> S. Michelin and O. Doaré, "Energy harvesting efficiency of piezoelectric flags in axial flows," *J. Fluid Mech.* **714**, 489–504 (2013).
- <sup>28</sup> Y. Xia, S. Michelin, and O. Doaré, "Fluid–solid–electric lock-in of energy-harvesting piezoelectric flags," *Phys. Rev. Appl.* **3**, 014009 (2015).
- <sup>29</sup> C. Li, E. J. Chae, Y. L. Young, X. Wang, and S. Alben, "Passive vibration control of flexible hydrofoils using piezoelectric material," in *Fourth International Symposium on Marine Propulsors* (SMP, Austin, Texas, USA, 2015), pp. 3123–3129.
- <sup>30</sup> S. Alben, "Simulating the dynamics of flexible bodies and vortex sheets," *J. Comput. Phys.* **228**(7), 2587–2603 (2009).

- <sup>31</sup> J. X. Sheng, A. Ysasi, D. Kolomenskiy, E. Kanso, M. Nitsche, and K. Schneider, "Simulating vortex wakes of flapping plates," in *Natural Locomotion in Fluids and on Surfaces* (Springer, 2012), pp. 255–262.
- <sup>32</sup> K. Singh, S. Michelin, and E. De Langre, "The effect of non-uniform damping on flutter in axial flow and energy-harvesting strategies," in *Proceedings of the Royal Society of London A: Mathematical, Physical and Engineering Sciences* (The Royal Society, 2012), Vol. 468, pp. 3620–3635.
- <sup>33</sup> W.-X. Huang and H. J. Sung, "Three-dimensional simulation of a flapping flag in a uniform flow," *J. Fluid Mech.* **653**, 301–336 (2010).
- <sup>34</sup> F. Tian, X. Lu, and H. Luo, "Onset of instability of a flag in uniform flow," *Theor. Appl. Mech. Lett.* **2**(2), 022005 (2012).
- <sup>35</sup> A. Erturk and D. J. Inman, "An experimentally validated bimorph cantilever model for piezoelectric energy harvesting from base excitations," *Smart Mater. Struct.* **18**(2), 025009 (2009).
- <sup>36</sup> N. E. DuToit and B. L. Wardle, "Experimental verification of models for microfabricated piezoelectric vibration energy harvesters," *AIAA J.* **45**(5), 1126–1137 (2007).
- <sup>37</sup> P. Bisegna, G. Caruso, and F. Maceri, "Optimized electric networks for vibration damping of piezoactuated beams," *J. Sound Vib.* **289**(4), 908–937 (2006).
- <sup>38</sup> Q.-M. Wang and L. E. Cross, "Constitutive equations of symmetrical triple layer piezoelectric benders," *IEEE Trans. Ultrason., Ferroelectrics Freq. Control* **46**(6), 1343–1351 (1999).
- <sup>39</sup> A. Erturk, W. G. R. Vieira, C. De Marqui, Jr., and D. J. Inman, "On the energy harvesting potential of piezoaeroelastic systems," *Appl. Phys. Lett.* **96**(18), 184103 (2010).
- <sup>40</sup> N. I. Muskhelishvili, *Singular Integral Equations: Boundary Problems of Function Theory and their Application to Mathematical Physics* (Courier Corporation, 2008).
- <sup>41</sup> R. Krasny, "Desingularization of periodic vortex sheet roll-up," *J. Comput. Phys.* **65**(2), 292–313 (1986).
- <sup>42</sup> S. Alben, "Regularizing a vortex sheet near a separation point," *J. Comput. Phys.* **229**(13), 5280–5298 (2010).
- <sup>43</sup> G. Birkhoff, "Helmholtz and Taylor instability," in *Proceedings of Symposia in Applied Mathematics* (American Mathematical Society, 1962), Vol. 13, pp. 55–76.
- <sup>44</sup> N. Rott, "Diffraction of a weak shock with vortex generation," *J. Fluid Mech.* **1**(1), 111–128 (1956).
- <sup>45</sup> T. Y. Hou, J. S. Lowengrub, and M. J. Shelley, "Boundary integral methods for multicomponent fluids and multiphase materials," *J. Comput. Phys.* **169**(2), 302–362 (2001).
- <sup>46</sup> S. Alben, "The attraction between a flexible filament and a point vortex," *J. Fluid Mech.* **697**, 481–503 (2012).
- <sup>47</sup> M. A. Jones, "The separated flow of an inviscid fluid around a moving flat plate," *J. Fluid Mech.* **496**, 405–441 (2003).
- <sup>48</sup> A. Ralston and P. Rabinowitz, *A First Course in Numerical Analysis* (Courier Corporation, 2012).
- <sup>49</sup> D. J. Acheson, *Elementary Fluid Dynamics* (Oxford University Press, 1990).
- <sup>50</sup> V. Adams and A. Askenazi, *Building Better Products with Finite Element Analysis* (Cengage Learning, 1999).
- <sup>51</sup> M. Chen, L.-B. Jia, Y.-F. Wu, X.-Z. Yin, and Y.-B. Ma, "Bifurcation and chaos of a flag in an inviscid flow," *J. Fluids Struct.* **45**, 124–137 (2014).
- <sup>52</sup> H. D. Akaydin, N. Elvin, and Y. Andreopoulos, "Energy harvesting from highly unsteady fluid flows using piezoelectric materials," *J. Intell. Mater. Syst. Struct.* **21**(13), 1263–1278 (2010).